Recent Hydrodynamic Modeling Enhancements in OpenFAST

Preprint

Lu Wang,[1] Jason Jonkman,[1] Greg Hayman,[2] Andy Platt,[1] Bonnie Jonkman,[3] and Amy Robertson[1]

1 National Renewable Energy Laboratory
2 Hayman Consulting LLC
3 Envision Energy

Presented at the 4th International Offshore Wind Technical Conference
Boston, Massachusetts
December 7–8, 2022

NREL is a national laboratory of the U.S. Department of Energy
Office of Energy Efficiency & Renewable Energy
Operated by the Alliance for Sustainable Energy, LLC

This report is available at no cost from the National Renewable Energy Laboratory (NREL) at www.nrel.gov/publications.

Contract No. DE-AC36-08GO28308

Conference Paper
NREL/CP-5000-83679
December 2022

Recent Hydrodynamic Modeling Enhancements in OpenFAST

Preprint

Lu Wang,[1] Jason Jonkman,[1] Greg Hayman,[2] Andy Platt,[1] Bonnie Jonkman,[3] and Amy Robertson[1]

1 National Renewable Energy Laboratory
2 Hayman Consulting LLC
3 Envision Energy

Suggested Citation
Wang, Lu, Jason Jonkman, Greg Hayman, Andy Platt, Bonnie Jonkman, and Amy Robertson. 2022. *Recent Hydrodynamic Modeling Enhancements in OpenFAST: Preprint*. Golden, CO: National Renewable Energy Laboratory. NREL/CP-5000-83679. https://www.nrel.gov/docs/fy23osti/83679.pdf.

NREL is a national laboratory of the U.S. Department of Energy
Office of Energy Efficiency & Renewable Energy
Operated by the Alliance for Sustainable Energy, LLC

This report is available at no cost from the National Renewable Energy Laboratory (NREL) at www.nrel.gov/publications.

Contract No. DE-AC36-08GO28308

Conference Paper
NREL/CP-5000-83679
December 2022

National Renewable Energy Laboratory
15013 Denver West Parkway
Golden, CO 80401
303-275-3000 • www.nrel.gov

NOTICE

This work was authored in part by the National Renewable Energy Laboratory, operated by Alliance for Sustainable Energy, LLC, for the U.S. Department of Energy (DOE) under Contract No. DE-AC36-08GO28308. Funding provided by the U.S. Department of Energy Office of Energy Efficiency and Renewable Energy Wind Energy Technologies Office. The views expressed herein do not necessarily represent the views of the DOE or the U.S. Government. The U.S. Government retains and the publisher, by accepting the article for publication, acknowledges that the U.S. Government retains a nonexclusive, paid-up, irrevocable, worldwide license to publish or reproduce the published form of this work, or allow others to do so, for U.S. Government purposes.

This report is available at no cost from the National Renewable Energy Laboratory (NREL) at www.nrel.gov/publications.

U.S. Department of Energy (DOE) reports produced after 1991 and a growing number of pre-1991 documents are available free via www.OSTI.gov.

Cover Photos by Dennis Schroeder: (clockwise, left to right) NREL 51934, NREL 45897, NREL 42160, NREL 45891, NREL 48097, NREL 46526.

NREL prints on paper that contains recycled content.

RECENT HYDRODYNAMIC MODELING ENHANCEMENTS IN OPENFAST

Lu Wang[1], Jason Jonkman[1], Greg Hayman[2], Andy Platt[1], Bonnie Jonkman[3], Amy Robertson[1]

[1] National Renewable Energy Laboratory, Golden, CO
[2] Hayman Consulting LLC, Boulder, CO
[3] Envision Energy USA Ltd., Boulder, CO

ABSTRACT

To improve the hydrodynamic modeling capabilities of the offshore wind design and modeling tool OpenFAST, a restructuring of the HydroDyn hydrodynamics module was undertaken with several new features implemented. The generation of the wave field is now separated from HydroDyn into a new module called SeaState. Unlike previous versions of HydroDyn, which precomputed the wave kinematics at the undisplaced positions of the hydrodynamic nodes, the new SeaState module computes the complete time history of the wave field at the vertices of a user-defined wave grid. During the simulation, the wave kinematics at any point within the grid can be efficiently interpolated, allowing the strip-theory wave loads to be evaluated based on the wave kinematics at the displaced structure position. A phase correction was also implemented for the potential-flow wave-exciting loads to account for large structure displacements. Several wave-stretching methods were implemented for the strip-theory solution along with a wave-load redistribution method that ensures smooth variation of the nodal loads as the nodes of a discrete hydrodynamic mesh enter and exit the water. The load smoothing is included to avoid the excitation of unphysical high-frequency structural vibration during hydroelastic simulations. The MacCamy-Fuchs diffraction correction for the strip-theory solution and the capability to insert a constrained NewWave into extreme stochastic sea states with directional spreading were also added. The present article documents the formulations of the new improvements to HydroDyn with example applications and numerical results.

Keywords: OpenFAST, HydroDyn, nonlinear, wave stretching, constrained wave, MacCamy-Fuchs, instantaneous position

1. INTRODUCTION

OpenFAST [1] is a widely used open-source engineering tool for coupled nonlinear time-domain aero-hydro-servo-elastic simulations of both onshore and offshore wind turbines developed by the National Renewable Energy Laboratory (NREL) through support from the U.S. Department of Energy. Despite its overall successful application to the modeling of distinct designs of fixed and floating offshore wind systems (see, e.g., Ref. [2, 3]), the previous implementation of the hydrodynamic module of OpenFAST, HydroDyn, involved several simplifications that could adversely impact the accuracy of the hydrodynamic modeling.

In the previous versions of HydroDyn, a major simplification to the evaluation of strip-theory fluid-inertia forces and viscous drag forces on the offshore wind substructure was the use of wave kinematics at the undisplaced reference position of the structure. This simplification was made to enable efficient evaluation of wave kinematics using inverse discrete Fourier transform (IDFT) in a preprocessing step before the start of the time-domain simulation. However, when modeling floating offshore wind turbines, this simplification, which also impacted the lumped axial fluid-inertia and drag forces applied at the end nodes of structural members, potentially results in large phase errors in the wave loads when large floater excursion in the horizontal plane caused by wind turbine thrust and/or resonance slow-drift motion exists. Similar issues were also present for structural members modeled with potential-flow solutions because the wave-exciting force and moment on the structure were also evaluated during preprocessing using IDFT and the wave spectrum at the undisplaced structure reference point (usually the origin).

Another limitation of the previous versions of HydroDyn was that the strip-theory hydrodynamic loads were always evaluated up to the still water level (SWL) instead of the instantaneous free surface. The lack of wave-stretching capabilities since the transition from FAST v7 to OpenFAST caused HydroDyn to underestimate the loads and responses of the offshore wind substructure in severe and extreme sea states. Furthermore, the Offshore Code Comparison Collaboration Continued with Correlation and unCertainty (OC6) project [4] showed that computing the strip-theory drag force with wave stretching up to the instantaneous free surface is critical for the prediction of nonlinear, low-frequency wave loads and the resulting slow-drift motion of semisubmersible offshore wind platforms [5]. The challenge that prevented a robust implementation of wave stretching in HydroDyn up until now was the discontinuous nodal wave loads caused by the abrupt jump from or to zero as a node enters or emerges from the water. Such discontinuous wave loads can result in a wideband excitation that potentially induces unphysical high-frequency structural vibration in hydroelastic simulations with the SubDyn module of OpenFAST.

Finally, features such as the ability to embed a large, constrained wave [6, 7] in a stochastically generated wave field and the MacCamy-Fuchs diffraction correction for short waves or large-diameter members [8] were absent from the previous implementation of HydroDyn. The former is a requirement for design load cases involving severe or extreme sea states by the IEC 61400-3-1 design standard for bottom-fixed offshore wind turbines [9].

To address the above limitations of HydroDyn and better support standards-based loads analysis with OpenFAST, an

This report is available at no cost from the National Renewable Energy Laboratory (NREL) at www.nrel.gov/publications.

overhaul of the HydroDyn module was undertaken with several new features implemented. The present article documents the formulations of the new improvements with example applications and numerical results. The improved hydrodynamic modeling in OpenFAST will be made publicly available in the near future.[1]

2. WAVE LOADS ON A DISPLACED STRUCTURE

Within OpenFAST, HydroDyn was originally responsible for the generation of the incident wave field and the evaluation of the hydrodynamic loads on the offshore wind substructure. HydroDyn models the substructure as a system of cylindrical members (possibly tapered), and each member is discretely represented using equally spaced nodes along the centerline of the member. All HydroDyn members fall under two categories: strip-theory members and hybrid members. For strip-theory members, distributed fluid-inertia forces proportional to the fluid acceleration, added-mass forces proportional to the structure acceleration, quadratic viscous drag forces based on the relative velocity, and hydrostatic loads are evaluated at the member nodes. Hybrid members, on the other hand, are modeled by linear or second-order potential-flow solutions, which provide the wave-exciting, wave-radiation, and hydrostatic loads on the structure. Therefore, only the distributed viscous drag force is evaluated at the member nodes for hybrid members. It is also possible to compute lumped axial fluid-inertia, added-mass, and viscous drag forces at the two end nodes of a member, with only the drag force being applicable to hybrid members. The hydrodynamic forces and moments on the HydroDyn members are subsequently summed about the structure reference point and passed to the 6-degrees-of-freedom rigid-body motion solver of the ElastoDyn module in the case of a rigid structure or mapped as distributed loads to the structural mesh of the SubDyn module in the case of a flexible body.

To enable the evaluation of wave loads considering wave kinematics at the instantaneous displaced position of the structure instead of the reference position, the generation of the incident wave field has been separated out from HydroDyn into a new module of OpenFAST called SeaState. The new SeaState module has all existing features from the previous versions of HydroDyn, including the options to include second-order sum- and difference-frequency wave components, wave directional spreading, and a depth-dependent current. Furthermore, a new feature allowing the user to insert a constrained NewWave group into irregular seas with possible second-order wave components and directional spreading was added to SeaState (see Section 4).

2.1 Strip-theory members

Previously, HydroDyn precomputed the wave kinematics and wave-exciting/fluid-inertia loads with the structure at the reference position before the start of the time-domain simulation. This approximation could potentially result in large phase errors in the wave loads especially for floating wind platforms when there is a large displacement in the horizontal plane caused by rotor thrust and/or low-frequency surge and sway resonance excited by nonlinear, difference-frequency wave loads [4].

The new SeaState module addresses this issue by precomputing the complete time series of wave kinematics—including wave elevation, fluid acceleration, fluid velocity, and dynamic pressure—at the vertices of a user-specified 3D wave grid. This wave grid is uniform in the horizontal x- and y-directions and cosine-spaced in the vertical z-direction to obtain finer resolution near the free surface. The range and number of grid points in each direction can be specified by the user. During the simulation, linear interpolation in space and time is performed for each node of the hydrodynamic mesh at each time step to efficiently obtain the relevant wave-field variables at the instantaneous displaced position of the structure, which are used to compute the wave-exciting/fluid-inertia force and viscous drag force on the structure following the standard strip-theory formulation (the former is only relevant to strip-theory members, whereas the latter is computed for both strip-theory members and hybrid members modeled with potential-flow solutions).

In HydroDyn, the wave loads on nodes out of water are zeroed. To avoid discontinuous wave loads on the hydrodynamic nodes as they enter or exit the water, which could potentially excite non-physical high-frequency structural vibration when the hydroelastic SubDyn module of OpenFAST is enabled, only the x- and y-displacements of the nodes are considered during the interpolation of wave kinematics without wave stretching, while the z-displacement is neglected (the reference z-position of each node is used). This simplification is considered acceptable because a large displacement in the z-direction is typically not expected, and only horizontal displacements in the x- and y-directions can lead to phase errors in the wave loads. However, if wave stretching is enabled, displacements in all three directions are considered when interpolating the wave kinematics, and the discontinuous nodal loads caused by water entry and exit are made smooth with a load-redistribution method (see Section 3).

2.2 Hybrid members

Previous versions of HydroDyn also precomputed the potential-flow wave-exciting loads on hybrid members using IDFT based on the incident wave spectrum at the structure reference point (usually the origin) and the frequency-domain linear potential-flow solution. Optional contributions from second-order sum- and difference-frequency wave-load quadratic transfer functions can also be included.

To account for the phase shift in the first-order wave-exciting loads caused by possible large structure displacement in the horizontal plane, the new implementation of HydroDyn precomputes multiple sets of wave-exciting load time series with the structure centered at different x- and y-positions in the wave field. This is achieved by performing IDFTs using the complex wave amplitude spectra at all free-surface nodes of the wave grid generated by SeaState. The first-order wave-exciting

[1] OpenFAST is available from https://github.com/OpenFAST/openfast.

This report is available at no cost from the National Renewable Energy Laboratory (NREL) at www.nrel.gov/publications.

force/moment in the m-th mode with the structure reference point at the grid point (x_j, y_k) at time t is given by

$$F_{ex,m}^{(1)}(t; x_j, y_k) = \Re\left\{\sum_{n=1}^{N} A_n(x_j, y_k) X_m^{(1)}(\omega_n, \beta_n) \mathrm{e}^{\mathrm{i}\omega_n t}\right\}, \quad (1)$$

where $A_n(x_j, y_k)$ is the complex amplitude of the wave component with frequency ω_n and heading β_n at the grid point. $X_m^{(1)}$ is the unit-amplitude wave-exciting force/moment in mode m from the linear potential-flow solution. Following linear wave theory, we can obtain $A_n(x_j, y_k)$ as

$$A_n(x_j, y_k) = A_{n,0} \mathrm{e}^{-\mathrm{i}k_n(x_j \cos\beta_n + y_k \sin\beta_n)}, \quad (2)$$

where $A_{n,0}$ and k_n are the complex amplitude at the origin and the wave number of the wave component with frequency ω_n and heading β_n, respectively.

During the time-domain simulation, the instantaneous wave-exciting loads on the structure are trilinearly interpolated from the different sets of wave-load time series, $F_{ex,m}^{(1)}(t; x_j, y_k)$, based on the x- and y-positions of the displaced structure reference point within the grid, $\left(x_{ref}(t), y_{ref}(t)\right)$.

If load contributions from second-order potential-flow solution are included in the model, the quadratic interactions of the first-order structural motion might already be accounted for in the second-order potential-flow quadratic transfer functions. To avoid double-counting the contribution from first-order motions, an optional low-pass filter for the floater motion was implemented to remove the linear response in the wave-frequency range, allowing the wave-load interpolation to be only based on any constant and/or nonlinear, low-frequency displacements, $(\tilde{x}_{ref}, \tilde{y}_{ref})$. The low-pass filtered reference x-position at the m-th time step is given by a recursive, single-pole filter with exponential smoothing, implemented in discrete time:

$$\tilde{x}_{ref}^{m} = C_{lo}\tilde{x}_{ref}^{m-1} + (1 - C_{lo})x_{ref}^{m}, \quad (3)$$

where the filter constant, C_{lo}, can be determined from the time step, Δt, and the user-specified cutoff frequency, f_{cutoff}:

$$C_{lo} = \mathrm{e}^{-2\pi\Delta t \cdot f_{cutoff}}. \quad (4)$$

The y-position of the structure is similarly filtered. This first-order filter is chosen to minimize the unwanted phase shift in the low-pass filtered displacement.

Alternatively, a band-pass filter can be used to only remove the wave-frequency motion while keeping the low- and high-frequency motion of the structure for interpolating the wave loads. However, high-frequency motion generally does not lead to large displacements that can cause appreciable phase error in the linear wave loads; therefore, a low-pass filter is deemed adequate and was implemented instead of a band-pass filter.

The potential-flow radiation loads are unaffected by the phase correction. On the other hand, the viscous drag force on hybrid members of the structure is evaluated in the same fashion as for strip-theory members described in Section 2.1. The wave-field velocity needed to compute the drag force is interpolated from the wave grid using the instantaneous displaced position of the hydrodynamic nodes.

3. WAVE STRETCHING WITH LOAD SMOOTHING

An in-depth validation study into the low-frequency resonance motion of semisubmersible offshore wind platforms was carried out during Phase I of the OC6 project under the International Energy Agency Wind Task 30 framework [4, 10]. One of the main conclusions from the study is that the transverse drag on surface-piercing columns plays a major role in the low-frequency wave excitation in surge and sway and the resulting resonance slow-drift motion of the structure. To accurately capture this effect, wave stretching must be included in the model [5]. As a result, wave-stretching capabilities have been formally implemented in HydroDyn.

Wave stretching is an extension to the strip-theory solution for both strip-theory and hybrid members (it only impacts the drag force on the latter). Wave stretching allows the wave kinematics and strip-theory hydrodynamic loads to be computed at all nodes within the fluid domain up to the instantaneous free-surface elevation given by $\zeta(t; x, y)$. In contrast, models without wave stretching compute wave kinematics and loads only at nodes between the seabed and the SWL regardless of the instantaneous free-surface elevation. In the new HydroDyn implementation, wave stretching applies to the flow velocity, the flow acceleration, and the dynamic pressure of the wave field and the current velocity. Wave stretching affects the added-mass, fluid-inertia, buoyancy, and viscous-drag terms of the distributed loads along members and the lumped loads at the end joints.

Three wave-stretching models are currently implemented: vertical stretching, extrapolation stretching, and Wheeler stretching. With vertical stretching, the wave kinematics in a wave crest (above the SWL to the instantaneous free surface) are computed using values at the SWL. Wave kinematics below the SWL are not modified; however, the wave loads are only computed up to $\zeta(t; x, y) < 0$ in a wave trough.

With extrapolation stretching, the wave kinematics in a wave crest are linearly extrapolated from the values at the SWL based on the z-derivatives of the first-order wave kinematics at the SWL ($z = 0$). Wave kinematics below the SWL are not modified; however, the wave loads are only computed up to $\zeta(t; x, y) < 0$ in a wave trough. Note that the z-derivatives of the second-order wave kinematics are not included in the linear extrapolation, which is consistent with second-order theory [11]. Effectively, the second-order terms are vertically stretched. Likewise, the slope of the current profile is not included in the linear extrapolation, effectively resulting in the vertical stretching of the current terms as well.

Finally, Wheeler stretching is based on linearly remapping the wave kinematics and dynamic pressure previously defined between the seabed and the SWL, $z \in [-h, 0]$, to $z \in [-h, \zeta(t; x, y)]$, where h is the uniform water depth. In other words, the wave-field variables at a point (x, y, z) in the water are now given by those at (x, y, z') in the original unstretched wave field, where z' is given by

This report is available at no cost from the National Renewable Energy Laboratory (NREL) at www.nrel.gov/publications.

$$z' = h\frac{h+z}{h+\zeta(t;x,y)} - h. \tag{5}$$

With $z \in [-h, \zeta(t;x,y)]$, we have $z' \in [-h, 0]$.

3.1 Nodal load redistribution

In OpenFAST, the distributed strip-theory hydrodynamic loads on a member are computed by discretizing each member into elements of equal length, δl, separated by nodes. The distributed load per unit length of the member is evaluated at the nodal positions, and a linear variation of the distributed load over each element is assumed. For example, Figure 1a and Figure 1b show the elements and nodes of a surface-piercing member and the hydrodynamic load distribution along the member, respectively. The load over each element is subsequently integrated and distributed to its two end nodes. The lumped load at each node is provided as input to the SubDyn module for finite-element hydroelastic simulations or summed together as input to ElastoDyn for rigid-body simulations.

With all three wave-stretching models, the hydrodynamic load at a node will be discontinuous as the node enters or exits the water, at which point the nodal load is abruptly shifted from or to zero. The discontinuous loads could potentially excite unphysical high-frequency structural vibration during hydroelastic simulations with SubDyn. To avoid this problem, a load-redistribution method was developed, which modifies the loads at the first and second nodes at or below the free surface in a fashion that maintains the total force and ensures the smoothness of the nodal loads.

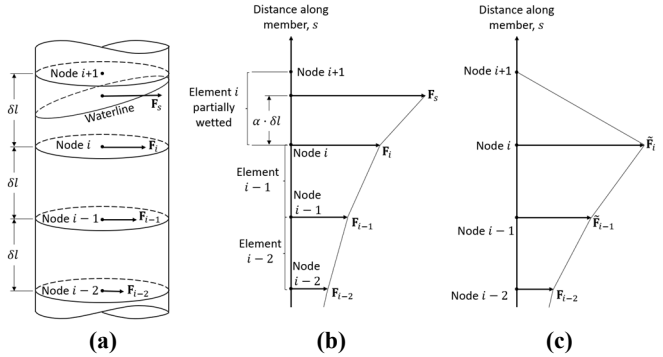

FIGURE 1: MODIFICATION TO THE DISTRIBUTED HYDRODYNAMIC LOADS NEAR THE WATERLINE. **(a)** ELEMENTS AND NODES OF A SURFACE-PIERCING HYDRODYNAMIC MEMBER NEAR THE FREE SURFACE. **(b)** UNMODIFIED LOAD DISTRIBUTION WITH WAVE STRETCHING. **(c)** MODIFIED LOAD DISTRIBUTION THAT GUARANTEES CONTINUITY AND SMOOTHNESS OF THE NODAL LOADS.

The load redistribution is illustrated in Figure 1b and Figure 1c. More specifically, the distributed strip-theory forces $\mathbf{F}_i$ and $\mathbf{F}_{i-1}$ (representing fluid-inertia force, added-mass force, or viscous drag force) at the first two nodes at or below the instantaneous free surface are modified to

$$\tilde{\mathbf{F}}_i = \mathbf{F}_i + \Delta\mathbf{F}_1(\alpha, \mathbf{F}_i, \mathbf{F}_s), \tag{6}$$

$$\tilde{\mathbf{F}}_{i-1} = \mathbf{F}_{i-1} + \Delta\mathbf{F}_2(\alpha, \mathbf{F}_i), \tag{7}$$

where $\Delta\mathbf{F}_1$ and $\Delta\mathbf{F}_2$ are the force modifications to the first and second nodes at or below the free surface, respectively. The force modifications depend on $\alpha \in [0,1)$, the fraction of element i that is wetted, the unmodified distributed force at the first node at or below the free surface, $\mathbf{F}_i$, and the unmodified distributed force at the intersection between the free surface and element i, $\mathbf{F}_s$ (see Figure 1).

The forms of $\Delta\mathbf{F}_1$ and $\Delta\mathbf{F}_2$ were developed to satisfy four numerical constraints:

1. The instantaneous total hydrodynamic force on the member must be maintained. In other words, the load distributions shown in Figure 1b and 1c should yield the same total force.
2. Any node above the instantaneous free surface, e.g., Node $i+1$ in Figure 1, should have zero hydrodynamic load.
3. The modified distributed load at each node must be continuous and smooth (continuous first derivative).
4. To minimize the impact of load redistribution, the load modification should be limited to only the first two nodes below the instantaneous waterline, Node i and Node $i-1$ in Figure 1.

For brevity, the details of the derivation are omitted here, and we only provide the final choices of $\Delta\mathbf{F}_1$ and $\Delta\mathbf{F}_2$, which are defined with the help of a polynomial smoothing function, $f(\alpha)$:

$$f(\alpha) = 2\alpha^3 - 3.5\alpha^2 + \alpha + 0.5. \tag{8}$$

$\Delta\mathbf{F}_1$ and $\Delta\mathbf{F}_2$ are given by

$$\Delta\mathbf{F}_1(\alpha, \mathbf{F}_i, \mathbf{F}_s) = \left(\frac{\alpha-1}{2} - f(\alpha)\right)\mathbf{F}_i + \frac{\alpha}{2}\mathbf{F}_s, \tag{9}$$

$$\Delta\mathbf{F}_2(\alpha, \mathbf{F}_i) = f(\alpha)\mathbf{F}_i. \tag{10}$$

Finally, because we have slightly modified the distribution of the hydrodynamic loads near the free surface, the total moment on the member is slightly altered. To correct the total moment, distributed moment corrections (moment per unit length), $\Delta\mathbf{M}_1(\alpha, \mathbf{F}_s)$ and $\Delta\mathbf{M}_2(\alpha, \mathbf{F}_i)$, should be added to the first and second nodes at or below the free surface, respectively:

$$\Delta\mathbf{M}_1(\alpha, \mathbf{F}_s) = \frac{\alpha^2 \cdot \delta l}{2}\mathbf{k} \times \mathbf{F}_s, \tag{11}$$

$$\Delta\mathbf{M}_2(\alpha, \mathbf{F}_i) = f(\alpha) \cdot \delta l \cdot \mathbf{k} \times \mathbf{F}_i, \tag{12}$$

where $\mathbf{k}$ is the unit vector along the centerline axis of the element. Note that the moment corrections are generally very small for fine member discretization and can often be negligible.

The lumped nodal forces and moments can simply be computed as $\delta l \cdot \tilde{\mathbf{F}}_i$ and $\delta l \cdot \Delta\mathbf{M}_i$, respectively, for the first two nodes at or below the instantaneous free surface or as $\delta l \cdot \mathbf{F}_i$ for other submerged nodes (no additional moment). The very first (deepest) node of the member is an exception; the lumped nodal force should be $\frac{\delta l}{2} \cdot \mathbf{F}_1$ to be consistent with the trapezoidal rule.

This report is available at no cost from the National Renewable Energy Laboratory (NREL) at www.nrel.gov/publications.

Any node above the free surface (starting from Node $i+1$ in Figure 1) has zero lumped nodal loads. Note that the load redistribution/smoothing requires the first (deepest) three nodes of the structural member to always remain submerged.

As an example, Figure 2 shows the modified (smoothed) and original (unsmoothed) distributed transverse drag force induced by a regular incident wave on a fixed vertical surface-piercing circular cylinder at two different nodes above and below the SWL. The incident wave has a period of 12 s and an amplitude of 3.7 m. For reference, Figure 2 also shows the submergence of each node, defined as the difference between the instantaneous free-surface elevation and the nodal elevation. A negative submergence indicates that the node is out of the water. As shown in Figure 2, the original unsmoothed transverse drag is discontinuous because the force is abruptly zeroed when the submergence becomes negative. In contrast, the modified transverse drag remains smooth throughout.

Figure 3 shows the power spectral densities (PSDs) of the distributed transverse drag force induced by irregular incident waves on the fixed cylinder at the two different nodes above and below the SWL. The incident wave is given by the Joint North Sea Wave Project (JONSWAP) spectrum with a peak period of 12 s, a significant wave height of 7 m, and a peak enhancement factor of 3.3. To demonstrate the effects of load smoothing, Figure 3 is zoomed in on the high-frequency excitation above the wave-frequency range. The high-frequency contents in the original (unsmoothed) drag force are absent from the modified (smoothed) force, indicating the load redistribution has achieved the desired effect.

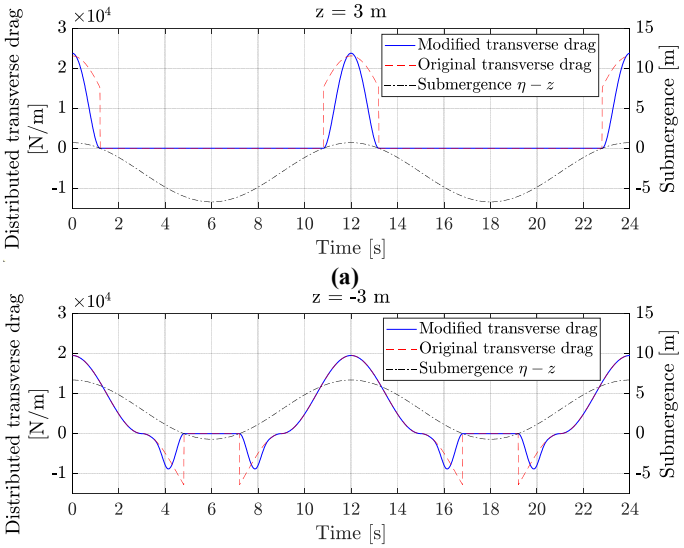

FIGURE 2: THE TRANSVERSE DRAG FORCE PER UNIT LENGTH ON A VERTICAL SURFACE-PIERCING CIRCULAR CYLINDER AT TWO DIFFERENT NODES ABOVE AND BELOW THE STILL-WATER LEVEL (SWL) INDUCED BY A REGULAR INCIDENT WAVE. **(a)** 3 m ABOVE THE SWL. **(b)** 3 m BELOW THE SWL.

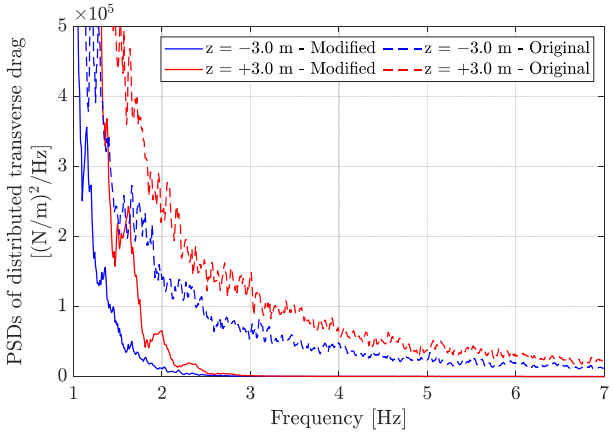

FIGURE 3: THE POWER SPECTRAL DENSITIES (PSD) OF THE TRANSVERSE DRAG FORCE PER UNIT LENGTH ON A VERTICAL SURFACE-PIERCING CIRCULAR CYLINDER AT TWO DIFFERENT NODES 3 m ABOVE AND BELOW THE SWL INDUCED BY IRREGULAR INCIDENT WAVES.

3.2 Hydrostatic loads on the exact wetted surface

In previous versions of HydroDyn without wave stretching, the hydrostatic loads on strip-theory members were computed exactly based on the instantaneous displaced surface of the member assuming circular cross sections but only up to the SWL for surface-piercing members [12].

In conjunction with the implementation of wave stretching, the approach to computing distributed hydrostatic loads from Ref. [12] was also updated to integrate the hydrostatic pressure on the exact wetted surface up to the instantaneous free surface, again assuming circular member cross sections. With this updated implementation, the slope of the free surface is also accounted for, in addition to the wave elevation, when evaluating the hydrostatic loads; however, it is assumed that the length scale of the waterplane area is small compared to the wavelength so that the free surface can be treated as planar with a constant normal vector in the vicinity of the waterplane.

Finally, the load redistribution/smoothing method for the nodal hydrostatic loads presented in Ref. [12] is retained to avoid discontinuous local loads on the structure.

4. CONSTRAINED NEWWAVE METHOD

The constrained NewWave method of Taylor et al. [7] allows an extreme wave of prescribed wave elevation or wave height to be embedded in a stochastic wave field. Moreover, the temporal profile of the embedded extreme wave is conditioned on the underlying wave spectrum, so that the embedded wave is statistically indistinguishable from one generated "naturally" through many random wave realizations. Therefore, with the constrained NewWave capability, structural loads and responses induced by extreme wave events can be efficiently captured without having to resort to many simulations with random wave realizations. The ability to embed a constrained extreme wave is required by the IEC 61400-3-1 design standard for fixed-bottom offshore wind turbines [9] for load cases involving severe or extreme sea states.

This report is available at no cost from the National Renewable Energy Laboratory (NREL) at www.nrel.gov/publications.

The constrained NewWave method is based on the NewWave model of Tromans et al. [6], which gives the most probable temporal profile of a large wave crest of a specified elevation based on the underlying wave spectrum. Consider a random wave with wave elevation $\zeta(t)$ at the origin given by

$$\zeta(t) = \sum_{n=1}^{N} A_n \cos(\omega_n t) + B_n \sin(\omega_n t). \quad (13)$$

The real-valued amplitudes, A_n and B_n, are independent normal random variables with zero means and equal variance $\sigma_n^2 = S(\omega_n)\Delta\omega$ where $S(\omega_n)$ is the wave power spectral density and $\Delta\omega = \omega_i - \omega_{i-1}$. The total variance of $\zeta(t)$ is given by $\sigma^2 = \sum_{n=1}^{N} \sigma_n^2$.

The NewWave model states that for a wave crest occurring at time t_1 with wave elevation $\zeta(t_1) = \zeta_c$ and $\dot{\zeta}(t_1) = 0$, the temporal profile of the wave crest for large ζ_c, $\zeta_c > 2\sigma$ for realistic ocean wave spectra [7], is given by

$$\zeta(\tau) = \zeta_c p(\tau) + q(\tau), \quad (14)$$

where $\tau = t - t_1$ so that the crest occurs at $\tau = 0$ and $q(\tau)$ is a non-stationary, Gaussian random variable with zero mean. The standard deviation of $q(\tau)$ is zero at $\tau = 0$ and increases to σ as $|\tau|$ increases. $p(\tau)$ is the autocorrelation function of the wave elevation given by

$$p(\tau) = \sigma^{-2} \sum_{n=1}^{N} \sigma_n^2 \cos(\omega_n \tau). \quad (15)$$

The standard deviation of $q(\tau)$ is independent of ζ_c; therefore, for large crests, the deterministic part of the crest profile, $\zeta_d(\tau) = \zeta_c p(\tau)$, dominates the random part, $q(\tau)$, and the crest profile becomes more deterministic. The variance of $q(\tau)$ is given by:

$$\sigma_q^2 = \sigma^2 \left(1 - p(\tau)^2 - \frac{\dot{p}(\tau)^2}{\ell^2}\right), \quad (16)$$

where ℓ depends on the second spectral moment, m_2, of the wave spectrum:

$$\ell^2 \sigma^2 = m_2 = \sum_{n=1}^{N} \omega_n^2 S(\omega_n) \Delta\omega. \quad (17)$$

The constrained NewWave approach entails modifying a wave time trace generated with the conventional random-wave method locally by inserting a NewWave group of a prescribed crest elevation. The expectation and the standard deviation of the modified wave time series should be consistent with the NewWave model given by Eq. (14) and Eq. (16). The procedure of Taylor et al. [7] is summarized below.

The modified wave time trace, $\tilde{\zeta}(\tau)$, with crest of elevation ζ_c at time $\tau = 0$ can be constructed from the random wave $\zeta(\tau)$ as

$$\tilde{\zeta}(\tau) = \zeta(\tau) + Q f_c(\tau) + R f_s(\tau). \quad (18)$$

The deterministic time signals $f_c(\tau)$ and $f_s(\tau)$ have zero slope and zero value at $\tau = 0$, respectively, and are of the forms

$$f_c(\tau) = \sum_{n=1}^{N} c_n \cos(\omega_n \tau), \quad (19)$$

$$f_s(\tau) = \sum_{n=1}^{N} d_n \sin(\omega_n \tau). \quad (20)$$

The coefficients Q and R are random because of the dependence on the random wave amplitudes A_n and B_n. To have $\tilde{\zeta}(0) = \zeta_c$ and $\dot{\tilde{\zeta}}(0) = 0$, we can choose

$$Q = \frac{\zeta_c - \sum_{n=1}^{N} A_n}{c}, \quad (21)$$

$$R = \frac{-\sum_{n=1}^{N} \omega_n B_n}{d}, \quad (22)$$

where $c = \sum_{n=1}^{N} c_n$ and $d = \sum_{n=1}^{N} \omega_n d_n$.

The expectation of $\tilde{\zeta}(t)$ is given by

$$E\left[\tilde{\zeta}(\tau)\right] = \frac{\zeta_c}{c} f_c(\tau) \quad (23)$$

because $E[A_n] = E[B_n] = 0$. The variance of $\tilde{\zeta}(\tau)$ is also given by Taylor et al. [7]. To match the expected constrained wave elevation of Eq. (23) with the most probable crest profile of the NewWave model in Eq. (14), we can choose

$$f_c(\tau) = c p(\tau) = \sum_{n=1}^{N} \sigma_n^2 \cos(\omega_n \tau). \quad (24)$$

To match the variance of $\tilde{\zeta}(\tau)$ (see Ref. [7]) to the NewWave model in Eq. (16), we can choose

$$f_s(\tau) = -\frac{d}{\ell^2} \dot{p}(\tau) = \sum_{n=1}^{N} \omega_n \sigma_n^2 \sin(\omega_n \tau). \quad (25)$$

We have $c_n = \sigma_n^2$ and $d_n = \omega_n \sigma_n^2$. With the above choice of Q, R, $f_c(\tau)$, and $f_s(\tau)$, Eq. (18) gives the final wave time series consistent with the NewWave model.

Example applications of the constrained NewWave method are shown in Figure 4 and Figure 5. In Figure 4, a random wave (solid line) is modified to have a crest of 12 m at $\tau = 0$ (dashed line). Figure 5 shows multiple random wave realizations modified to have a crest of 12 m at $\tau = 0$, and the resulting distribution of wave elevation is also consistent with the NewWave model.

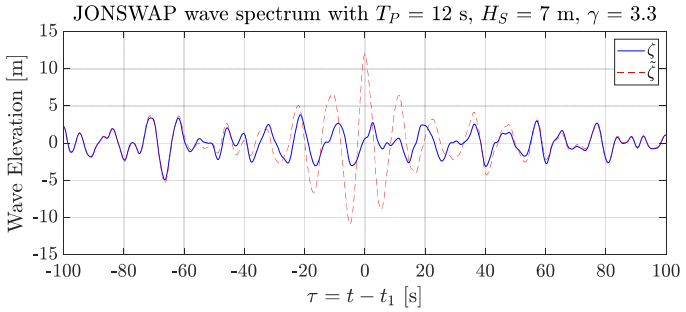

FIGURE 4: COMPARISON OF THE MODIFIED WAVE TIME TRACE, $\tilde{\zeta}(\tau)$, WITH A CONSTRAINED NEWWAVE GROUP OF CREST ELEVATION 12 m AND THE ORIGINAL RANDOM IRREGULAR WAVE, $\zeta(\tau)$.

This report is available at no cost from the National Renewable Energy Laboratory (NREL) at www.nrel.gov/publications.

In the present implementation of the constrained NewWave model in SeaState, the linear wave components are modified to obtain the user-defined crest elevation exactly at a user-specified time and location. The constrained NewWave feature is compatible with wave directional spreading and second-order wave kinematics; however, if second-order wave kinematics are enabled, the crest elevation could deviate from the specified value due to the addition of the difference- and/or sum-frequency wave components. In addition to specifying crest elevation, it is also possible to specify the crest height defined as the difference between the NewWave crest elevation and the trough immediately preceding or following the crest in time, whichever is deeper. SeaState will iterate on the crest elevation until the resulting crest height is within a relative tolerance of 10^{-3}. Figure 6 shows an example application of the constrained NewWave method to irregular seas with directional spreading and with the crest height specified.

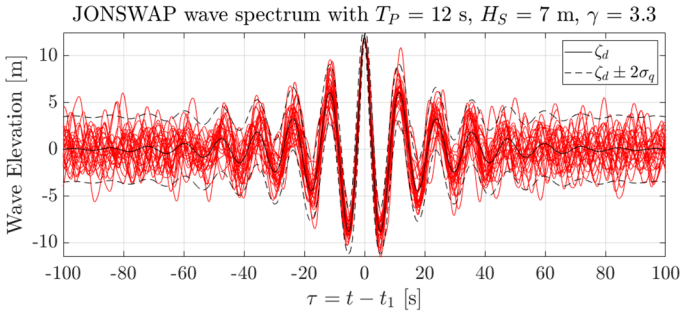

FIGURE 5: MULTIPLE WAVE REALIZATIONS (RED CURVES) WITH A CONSTRAINED NEWWAVE GROUP OF A TARGET CREST ELEVATION OF 12 m.

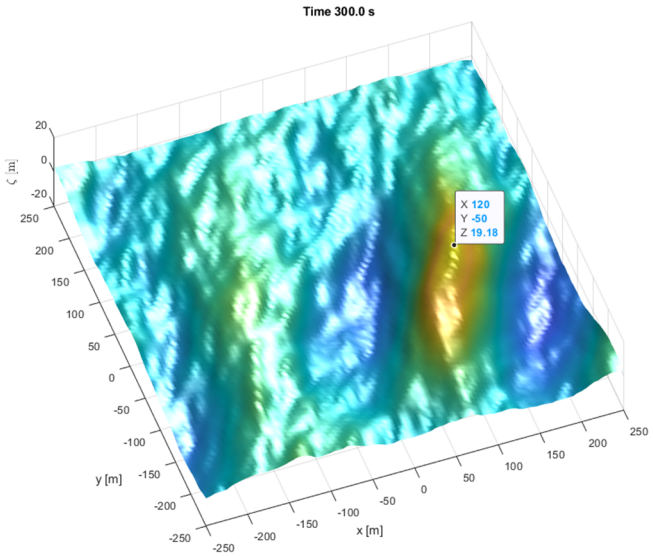

FIGURE 6: WAVE FIELD WITH DIRECTIONAL SPREADING AND A CONSTRAINED NEWWAVE GROUP. THE USER-SPECIFIED WAVE CREST IS AT TIME $t_1 = 300$ s AND LOCATION $x = 120$ m and $y = -50$ m. THE TARGET CREST HEIGHT OF 35 m RESULTS IN A CREST ELEVATION OF 19.18 m.

5. MACCAMY-FUCHS DIFFRACTION CORRECTION

The original Morison equation for strip-theory wave loads with a constant effective mass coefficient tends to overpredict the wave-exciting force when the wavelength becomes comparable to the body diameter due to nonnegligible wave-diffraction effects. This problem can be avoided by using potential-flow solution to predict the wave loads. However, potential-flow modeling is inconvenient for hydroelastic simulations where local hydrodynamic loads on structural members are needed. In this case, it is preferrable to have a strip-theory approximation that also accounts for wave-diffraction effects. This can be achieved, at least for vertical surface-piercing circular cylinders, through the MacCamy-Fuchs diffraction correction based on linear potential-flow theory.

Consider a bottom-mounted surface-piercing circular cylinder of radius a centered at $x = 0$ subjected to a regular long-crested incident wave in the x-direction of amplitude A, angular frequency ω, and wave number k. At $x = 0$, the center of the cylinder, the x-component of the flow acceleration of the incident wave field is

$$\dot{u} = \Re\left\{Akg\frac{\cosh\big(k(z+h)\big)}{\cosh(kh)}\mathrm{e}^{-\mathrm{i}\omega t}\right\}, \tag{26}$$

where g is the gravitational acceleration. The exact sectional diffraction load in the x-direction per unit height of the column is given by the linear potential-flow theory [8]:

$$F = \Re\left\{\mathrm{i}A\frac{4\rho g a}{ka}\frac{\cosh\big(k(z+h)\big)}{\cosh(kh)}\frac{\mathrm{e}^{-\mathrm{i}\omega t}}{H_1^{(1)\prime}(ka)}\right\}, \tag{27}$$

where ρ is the density of water and $H_1^{(1)\prime}$ is the derivative of the Hankel function of the first kind of order one. Assuming the sectional diffraction load is of the form of the acceleration term in the Morison equation, we have

$$F = \rho(\pi a^2)\dot{u}C_M, \tag{28}$$

where C_M is the effective mass coefficient. Matching Eq. (27) and Eq. (28), we can derive the following expression for the effective mass coefficient:

$$C_M(ka) = \frac{4\mathrm{i}}{\pi(ka)^2 H_1^{(1)\prime}(ka)}. \tag{29}$$

Figure 7 shows the magnitude and phase of C_M.

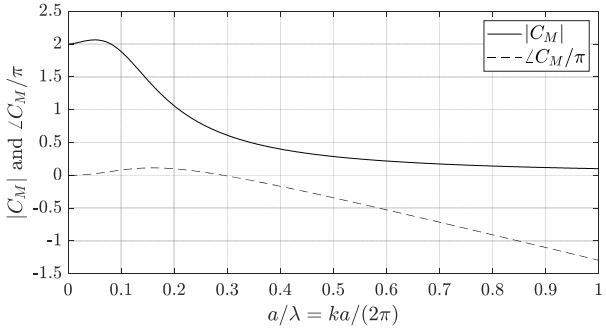

FIGURE 7: MAGNITUDE AND PHASE OF THE EXACT EFFECTIVE MASS COEFFICIENT, C_M.

This report is available at no cost from the National Renewable Energy Laboratory (NREL) at www.nrel.gov/publications.

When $a/\lambda < 0.4$, where λ is the wavelength, the phase of C_M is close to zero; the transverse wave load is mostly in phase with the flow acceleration. The wave load is small when $a/\lambda \geq 0.4$; therefore, we can approximate the wave load as being in phase with the flow acceleration, thus rendering C_M a real number:

$$C_M(ka) \approx \frac{4}{\pi(ka)^2 \left|H_1^{(1)'}(ka)\right|}. \quad (30)$$

In irregular waves, we have

$$F = \rho(\pi a^2) \sum_{n=1}^{N} \dot{u}_n C_M(k_n a), \quad (31)$$

where $\dot{u}_n$ is the x-component of the flow acceleration associated with the incident wave component of angular frequency ω_n. The effective mass coefficient, $C_M(k_n a)$, is a function of the product of the wave number k_n associated with the angular frequency ω_n and the column radius a.

In OpenFAST, the user typically specifies a constant added mass coefficient, C_A, and a constant pressure coefficient (associated with the pressure gradient in an unsteady flow field), C_P (default to 1), which leads to a constant effective mass coefficient equal to $C_M = C_A + C_P$. With, the MacCamy-Fuchs diffraction model, the effective mass coefficient based on the user input will be replaced by $C_M(k_n a)$ given by Eq. (30). Therefore, when the MacCamy-Fuchs diffraction correction is enabled, it is no longer necessary for the user to specify C_P, which is only used when computing the fluid-inertia forces proportional to the fluid acceleration. Note that the user can still specify C_A, which is used to compute the added-mass force proportional to the acceleration of the structure.

As discussed in Section 2.1, the flow acceleration is optionally evaluated at the instantaneous body position in the updated HydroDyn. Since the body position is generally not known a priori, the fluid-inertia forces cannot be evaluated beforehand and will have to be computed during the simulation using the instantaneous wave field. To conform to this new framework, it is convenient to absorb $C_M(k_n a)$ into the flow acceleration to obtain the modified flow acceleration, $\dot{\tilde{u}}$, which can be precomputed by SeaState:

$$F = \rho(\pi a^2)\, \dot{\tilde{u}}, \quad (32)$$

$$\dot{\tilde{u}}(t; x, y, z) = \sum_{n=1}^{N} \dot{u}_n(t; x, y, z) C_M(k_n a). \quad (33)$$

Since $C_M(k_n a)$ also depends on the member radius, we potentially need to compute and store a separate grid of $\dot{\tilde{u}}$ for each member with the MacCamy-Fuchs correction enabled because they can have different diameters. This will result in excessive memory use; therefore, in the present OpenFAST implementation, we require all members with the MacCamy-Fuchs correction enabled to have approximately the same diameter within $\pm 10\%$ of the nominal diameter of $2a$, where a is the radius used to compute the modified acceleration in Eq. (33). With this restriction, we only need to compute and store one additional grid for the modified flow acceleration, $\dot{\tilde{u}}$, in addition to the grid for the unmodified flow acceleration, $\dot{u}$, which is still required to evaluate the fluid-inertia forces on members without the MacCamy-Fuchs model enabled, and to evaluate axial fluid-inertia forces at the end joints of members.

In the HydroDyn implementation, Eq. (32) and Eq. (33) are generalized for members that are not perfectly vertical with possible wave spreading. However, to ensure that the MacCamy-Fuchs diffraction solution is approximately valid, it can only be applied to surface-piercing members with an inclination within 10° from vertical. Furthermore, because the MacCamy-Fuchs model is based on the linear potential-flow theory, second-order fluid acceleration at the sum and difference frequencies are ignored when computing the transverse fluid-inertia forces for members with the MacCamy-Fuchs model enabled.

6. EXAMPLE RESULTS

To demonstrate the new modeling capabilities of SeaState and HydroDyn within OpenFAST, coupled aero-hydro-servo-elastic simulations of the IEA Wind 15-MW offshore reference wind turbine atop a monopile [13] and the VolturnUS-S reference platform were performed [14].

6.1 The IEA 15-MW reference wind turbine atop a monopile

First, the IEA 15-MW reference wind turbine atop a monopile [13] was simulated to demonstrate the effect of wave stretching in conjunction with a large constrained NewWave group. The MacCamy-Fuchs diffraction correction was also enabled for the flexible monopile, which was modeled using strip theory only. For this purpose, the condition described by Design Load Case 6.1 of the IEC 61400-3-1 standard [9] was selected. The extreme sea state was generated with the JONSWAP wave spectrum with a 50-year significant wave height of $H_{s50} = 10$ m and a peak period of $T_p = 14$ s. NREL's TurbSim tool was used to generate the nonuniform but spatially coherent turbulent wind field based on the extreme wind speed model with a 10-min average wind speed of 50 m/s at hub height (wind turbine class I [15]) and a Category B turbulence [15]. The power-law wind profile with an exponent of 0.11 was adopted [15]. Each simulation lasted 12 min, and the first 2 min of the time series were discarded as startup transient. After 7 min (420 s) from the start of the simulation, a large wave with the extreme individual wave height of $1.86 \cdot H_{s50}$ [9] was inserted using the constrained NewWave method. Aligned wind and waves were assumed without current. Consistent with [9], the turbine is idling with the blades at the feathered position in the simulation, but no nacelle misalignment was included for simplicity. Figure 8 compares the results obtained with the three different wave-stretching methods to that without wave stretching.

Without wave stretching, the maximum tower-base surge displacement occurs at 416 s immediately preceding the large, embedded wave crest at 420 s. In contrast, the maximum displacement occurs right after the embedded wave crest at 427 s when any of the wave-stretching method is enabled. The maximum mudline pitch bending moment always occurs at approximately 423 s right after the embedded wave crest.

This report is available at no cost from the National Renewable Energy Laboratory (NREL) at www.nrel.gov/publications.

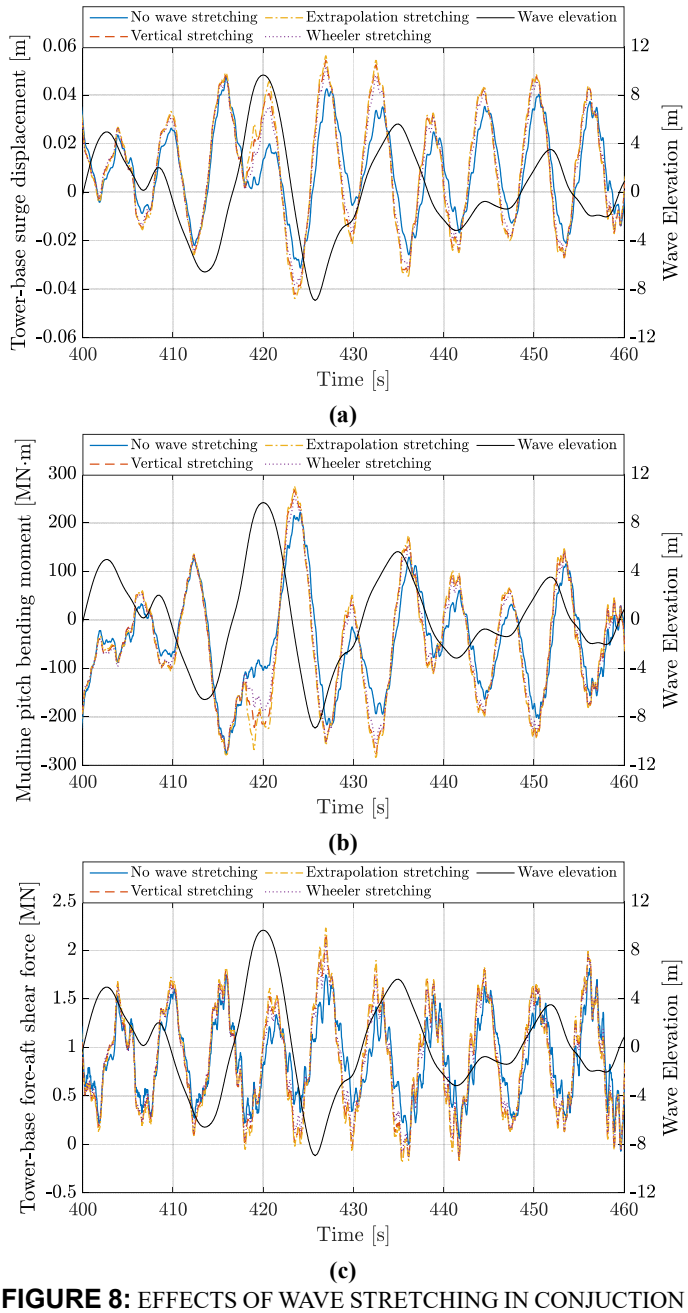

FIGURE 8: EFFECTS OF WAVE STRETCHING IN CONJUCTION WITH AN EMBEDDED EXTREME WAVE ON **(a)** THE TOWER-BASE SURGE DISPLACEMENT, **(b)** THE MUDLINE PITCH BENDING MOMENT, AND **(c)** THE TOWER-BASE FORE-AFT SHEAR FORCE OF THE IEA 15-MW REFERENCE WIND TURBINE ATOP A MONOPILE.

Finally, with wave stretching, the maximum tower-base fore-aft shear force is observed at 427 s, also immediately after the embedded wave crest but occurs long after the embedded wave crest at 456 s without wave stretching. This suggests that the full effect of the embedded wave on the tower-base loads is not captured without wave stretching. The maximum tower-base surge motion, mudline pitch moment, and tower-base fore-aft shear force with and without the various wave-stretching models are summarized in Table 1. The use of wave stretching substantially increases the selected loads and responses compared to without stretching. Furthermore, extrapolation stretching results in the highest increase, whereas Wheeler stretching leads to the lowest, as expected.

6.2 The IEA 15-MW reference wind turbine atop the VolturnUS-S reference platform

The second example is concerned with the IEA 15-MW reference wind turbine atop the VolturnUS-S reference semisubmersible platform [14]. This floating configuration was selected to demonstrate the effects of the phase correction for the wave loads using the displaced position of the structure. The wave-exciting and radiation loads on the semisubmersible were computed using the first-order and second-order sum- and difference-frequency potential-flow solutions with both distributed transverse and lumped axial drag forces. A depth-dependent transverse drag coefficient was used in conjunction with vertical wave stretching to better capture the slow-drift motion of the floating platform [5]. The phase of the first-order potential-flow wave-exciting force was corrected following Section 2.2 both with and without the low-pass filter, and the drag forces on the structure were evaluated based on the wave-field velocity at the displaced position of the structure.

The condition of Design Load Case 1.6 [9] with an operating wind turbine was chosen with an average wind speed of 12 m/s just above the rated wind speed, resulting in an average aerodynamic thrust of 1.6 MN. The wind field was again generated with TurbSim based on the normal turbulence model with a Category B turbulence and the power-law wind profile with an exponent of 0.14 [9]. The severe sea state was characterized by the JONSWAP spectrum with a significant wave height of 8.5 m and a peak period of 13.1 s. Aligned wind and waves with no current was assumed, and no nacelle misalignment was considered. The semisubmersible platform was assumed to be rigid here but can be modeled as flexible in the future with the SubDyn module of OpenFAST. The simulation lasted 70 min with the first 10 min discarded as startup transient.

TABLE 1: MAXIMUM MONOPILE LOADS AND RESPONSES ESTIMATED WITH AND WITHOUT WAVE STRETCHING.

Wave Stretching	Tower-base surge motion	Mudline pitch moment	Tower-base fore-aft shear force
None	0.047 m	222 MN·m	1.81 MN
Vertical	0.054 m	268 MN·m	2.17 MN
Extrap.	0.056 m	276 MN·m	2.23 MN
Wheeler	0.052 m	255 MN·m	2.07 MN

Figure 9 compares the results from the simulations with the wave loads evaluated at the reference undisplaced floater position and the instantaneous displaced floater position with and without low-pass filtering. As shown in Figure 9a, the

This report is available at no cost from the National Renewable Energy Laboratory (NREL) at www.nrel.gov/publications.

aerodynamic thrust on the wind turbine results in a mean surge offset of approximately 18 m. This mean offset leads to a small but discernible phase lag in the hydrodynamic surge force on the platform in Figure 9b when the wave loads are computed based on the offset position instead of the reference position. This phase lag is also visible with the wave-frequency surge motion in Figure 9a.

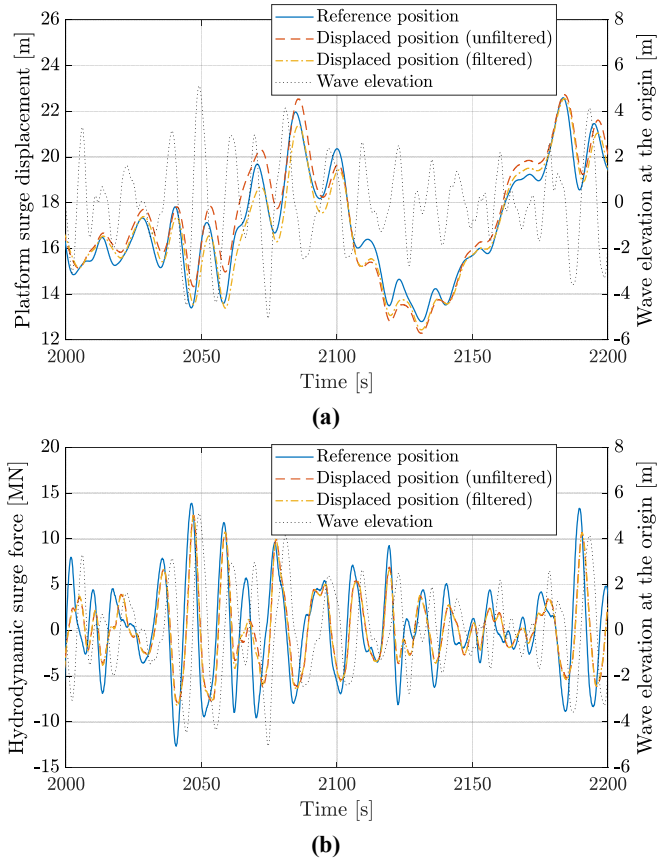

FIGURE 9: THE EFFECTS OF COMPUTING THE WAVE LOADS ON THE SEMISUBMERSIBLE PLATFORM AT THE DISPLACED POSITION OF THE STRUCTURE AS OPPOSED TO AT THE UN-DISPLACED REFERENCE POSITION. **(a)** PLATFORM SURGE MOTION. **(b)** HYDRODYNAMIC SURGE FORCE ON THE PLATFORM.

Figure 10 shows the PSDs of the platform surge motion. A distinct resonance peak at the low surge natural frequency of approximately 0.01 Hz is present in all solutions; however, computing the wave loads on the platform using the unfiltered displaced position of the structure also has the interesting effect of increasing the amplitude of the low-frequency surge resonance motion, resulting in a higher spectral peak. The increase in the PSD integrals over the low-frequency range (0.0025 Hz to 0.02 Hz), which is equal to the variance of the low-frequency motion, is 26% relative to the solution with the structure at the reference position (approximately a 12% difference in motion amplitude).

The increased low-frequency surge motion is likely a consequence of partially double-counting the quadratic interaction of the first-order structural motion as discussed in Section 2.2. This is supported by the fact that the low-frequency surge motion predicted using the low-pass filtered floater position (with a cutoff frequency of 0.04 Hz) is close to that with the structure at the undisplaced reference position in Figure 10. On the other hand, the motion filtering has little effect on the wave-frequency responses with the two solutions based on the displaced position of the floater with and without filtering being visually identical in Figure 10.

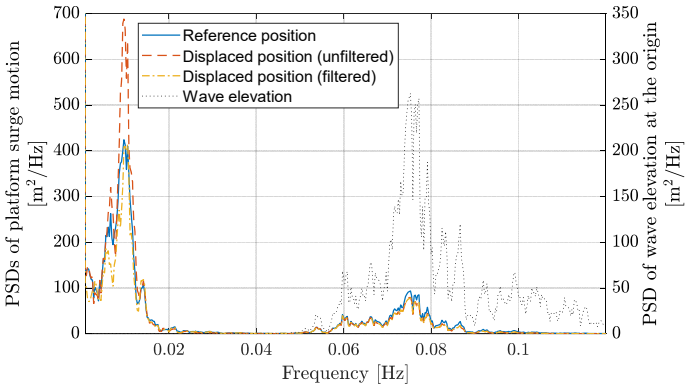

FIGURE 10: COMPARISON OF THE COMPUTED POWER SPECTRAL DENSITIES (PSD) OF THE PLATFORM SURGE MOTION. THE WAVE LOADS WERE EITHER COMPUTED WITH THE STRUCTURE AT THE UNDISPLACED REFERENCE POSITION OR AT THE INSTANTANEOUS DISPLACED POSITION WITH AND WITHOUT LOW-PASS FILTERING.

7. CONCLUSIONS

To improve the hydrodynamic modeling capabilities of OpenFAST, especially with nonlinear wave loadings, a major overhaul of the HydroDyn hydrodynamics module of OpenFAST was undertaken.

First, the generation of the incident wave field was separated from HydroDyn into an independent new module of OpenFAST called SeaState, which computes the complete time histories of wave kinematics at the vertices of a user-defined 3D wave grid. The wave grid allows the wave kinematics at any point within the grid to be evaluated efficiently using interpolation during the simulation, thus enabling the evaluation of strip-theory wave loads with the structure at its displaced position.

For hybrid models, a phase correction for the potential-flow wave-exciting loads on the structure was also implemented, where the wave-exciting loads on the structure is precomputed using inverse discrete Fourier transform with the structure centered at the vertices of a 2D horizontal grid. During the simulation, the instantaneous wave loads on the structure is interpolated based on the displaced position of the structure within the grid. To avoid double-counting the contributions from first-order motions to second-order wave loads when second-order potential-flow solution is included in the model, an optional low-pass filter for the floater motion was implemented to remove the linear response in the wave-frequency range when interpolating the wave loads.

This report is available at no cost from the National Renewable Energy Laboratory (NREL) at www.nrel.gov/publications.

Vertical, extrapolation, and Wheeler wave-stretching methods were also implemented in the updated HydroDyn module. A load-redistribution procedure was implemented to ensure continuous and smooth lumped wave loads at each discrete hydrodynamic node of the structure, even as the free surface moves past nodes. The smoothing of the loads prevents the excitation of unphysical high-frequency structural vibration in hydroelastic simulations with the SubDyn module of OpenFAST.

Finally, the capability to embed a constrained extreme wave in the stochastic incident waves based on the NewWave model and the MacCamy-Fuchs diffraction correction were implemented.

As examples, aero-hydro-servo-elastic simulations with OpenFAST were performed. The first example with the IEA Wind 15-MW reference wind turbine atop a monopile demonstrates the application of wave stretching in conjunction with a large, embedded wave. The use of wave stretching significantly increases the predicted loads and responses of the monopile induced by the large wave. The second example involving the IEA Wind reference turbine atop the VolturnUS-S reference platform demonstrates the effects of evaluating the wave loads on the structure based on its displaced position. The large mean surge displacement induced by the turbine thrust leads to a phase shift in both the wave loads and the surge motion of the structure. Because second-order potential-flow quadratic transfer functions are included in the model, interpolating the wave loads using the exact instantaneous position of the structure likely results in double-counting the contributions from first-order motion to second-order wave loads. As a result, the slow-drift motion increases substantially. By interpolating the wave loads using the low-pass filtered floater motion instead, the increase in the slow-drift motion is removed, while retaining the phase correction in wave-frequency wave loads and motion.

The new capabilities provided by the SeaState module and the updated HydroDyn module should greatly enhance the hydrodynamic modeling capabilities of OpenFAST in terms of nonlinear wave loads and facilitate standards-based loads analysis of fixed and floating offshore wind systems.

In the future, the constrained-wave capability of SeaState can be extended to fully support second-order wave components by iterating on the first-order crest elevation until the target crest elevation or crest height is achieved with contributions from second-order wave components.

ACKNOWLEDGEMENTS

This work was authored in part by the National Renewable Energy Laboratory, operated by Alliance for Sustainable Energy, LLC, for the U.S. Department of Energy (DOE) under Contract No. DE-AC36-08GO28308. Funding provided by the U.S. Department of Energy Office of Energy Efficiency and Renewable Energy Wind Energy Technologies Office. Support for the work was also provided by Envision Energy USA Ltd. under Agreement FIA-17-01834-3. The views expressed in the article do not necessarily represent the views of the DOE or the U.S. Government. The U.S. Government retains and the publisher, by accepting the article for publication, acknowledges that the U.S. Government retains a nonexclusive, paid-up, irrevocable, worldwide license to publish or reproduce the published form of this work, or allow others to do so, for U.S. Government purposes. A portion of this research was performed using computational resources sponsored by the U.S. Department of Energy's Office of Energy Efficiency and Renewable Energy and located at the National Renewable Energy Laboratory.

REFERENCES

[1] Jonkman, J.M., (2013), "The new modularization framework for the FAST wind turbine CAE tool," in *Proceedings of the 51st AIAA Aerospace Sciences Meeting including the New Horizons Forum and Aerospace Exposition*, Grapevine, TX, USA.

[2] Bergua, R., Robertson, A., Jonkman, J., Platt, A., Page, A., Qvist, J., Amet, E., Cai, Z., Han, H., Beardsell, A., et al. (2022), "OC6 phase II: Integration and verification of a new soil–structure interaction model for offshore wind design," *Wind Energy,* Vol. 25, No. 5, pp. 793-810.

[3] Thomsen, J.B., Bergua, R., Jonkman, J., Robertson, A., Mendoza, N., Brown, C., Galinos, C. and Stiesdal, H., (2021), "Modeling the TetraSpar floating offshore wind turbine foundation as a flexible structure in OrcaFlex and OpenFAST," *Energies,* Vol. 14, p. 7866.

[4] Robertson, A., Gueydon, S., Bachynski, E., Wang, L., Jonkman, J., Alarcón, D., Amet, E., Beardsell, A., Bonnet, P., Boudet, B., Brun, C., et al. (2020), "OC6 phase I: Investigating the underprediction of low-frequency hydrodynamic loads and responses of a floating wind turbine," *J. Phys.: Conf. Ser.,* Vol. 1618, No. 3, p. 032033.

[5] Wang, L., Robertson, A., Jonkman, J. and Yu, Y.-H., (2022), "OC6 phase I: Improvements to the OpenFAST predictions of nonlinear, low-frequency responses of a floating offshore wind turbine platform," *Renew. Energy,* Vol. 187, pp. 282-301.

[6] Tromans, P.S., Anaturk, A.R. and Hagemeijer, P., (1991), "A new model for the kinematics of large ocean waves—application as a design wave," in *Proceedings of the First International Offshore and Polar Engineering Conference*, Edinburgh, UK.

[7] Taylor, P.H., Jonathan, P. and Harland, L.A., (1997), "Time domain simulation of jack-up dynamics with the extremes of a Gaussian process," *J. Vib. Acoust.,* Vol. 119, pp. 624-628.

[8] MacCamy, R.C. and Fuchs, R.A., (1954), "Wave forces on piles: A diffraction theory," US Army Corps of Engineers, Beach Erosion Board.

[9] International Electrotechnical Commission, (2018), "IEC 61400-3-1 Wind energy generation systems – Part 3-1: Design requirements for fixed offshore wind turbines,"

This report is available at no cost from the National Renewable Energy Laboratory (NREL) at www.nrel.gov/publications.

International Electrotechnical Commission, Geneva, Switzerland.

[10] Wang, L., Robertson, A., Jonkman, J., Yu, Y.-H., Koop, A., Borràs Nadal, A., Li, H., Bachynski-Polić, E., Pinguet, R., Shi, W., et al. (2021), "OC6 phase Ib: Validation of the CFD predictions of difference-frequency wave excitation on a FOWT semisubmersible," *Ocean Eng.,* Vol. 241, p. 110026.

[11] Stansberg, C.T., Amundsen, A., Fouques, S. and Økland, O.D., (2013), "Second-order random wave kinematics and resulting loads on a bottom-fixed slender monopile," in *Proceedings of the ASME 2013 32nd International Conference on Ocean, Offshore and Arctic Engineering*, Nantes, France, p. V008T09A092.

[12] Jonkman, J., Branlard, E., Hall, M., Hayman, G., Platt, A. and Robertson, A., (2020), "Implementation of substructure flexibility and member-level load capabilities for floating offshore wind turbines in OpenFAST," National Renewable Energy Laboratory, Golden, CO, USA.

[13] Gaertner, E., Rinker, J., Sethuraman, L., Zahle, F., Anderson, B., Barter, G., Abbas, N., Meng, F., Bortolotti, P., Skrzypinski, W., et al., (2020), "Definition of the IEA 15-megawatt offshore reference wind turbine," National Renewable Energy Laboratory, Golden, CO, USA.

[14] Allen, C., Viselli, A., Dagher, H., Goupee, A., Gaertner, E., Abbas, N., Hall, M. and Barter, G., (2020), "Definition of the UMaine VolturnUS-S reference platform developed for the IEA Wind 15-megawatt offshore reference wind turbine," National Renewable Energy Laboratory, Golden, CO, USA.

[15] International Electrotechnical Commission, (2019), "IEC 61400-1 Wind energy generation systems - Part 1: Design requirements," International Electrotechnical Commission, Geneva, Switzerland.

This report is available at no cost from the National Renewable Energy Laboratory (NREL) at www.nrel.gov/publications.